
BRAIN-INSPIRED ONLINE ADAPTATION FOR REMOTE SENSING WITH SPIKING NEURAL NETWORK

A PREPRINT

Dexin Duan*

Peilin Liu*

Fei Wen* [†]

ABSTRACT

On-device computing, or edge computing, is becoming increasingly important for remote sensing, particularly in applications like deep network-based perception on on-orbit satellites and unmanned aerial vehicles (UAVs). In these scenarios, two brain-like capabilities are crucial for remote sensing models: (1) *high energy efficiency*, allowing the model to operate on edge devices with limited computing resources, and (2) *online adaptation*, enabling the model to quickly adapt to environmental variations, weather changes, and sensor drift. This work addresses these needs by proposing an online adaptation framework based on spiking neural networks (SNNs) for remote sensing. Starting with a pretrained SNN model, we design an efficient, unsupervised online adaptation algorithm, which adopts an approximation of the BPTT algorithm and only involves forward-in-time computation that significantly reduces the computational complexity of SNN adaptation learning. Besides, we propose an adaptive activation scaling scheme to boost online SNN adaptation performance, particularly in low time-steps. Furthermore, for the more challenging remote sensing detection task, we propose a confidence-based instance weighting scheme, which substantially improves adaptation performance in the detection task. To our knowledge, this work is the first to address the online adaptation of SNNs. Extensive experiments on seven benchmark datasets across classification, segmentation, and detection tasks demonstrate that our proposed method significantly outperforms existing domain adaptation and domain generalization approaches under varying weather conditions. The proposed method enables energy-efficient and fast online adaptation on edge devices, and has much potential in applications such as remote perception on on-orbit satellites and UAV.

Keywords Unsupervised domain adaptation · brain-inspired computing · remote sensing image processing · neuromorphic computing · spiking neural network (SNN)

1 Introduction

In the past a few years, benefited from the rapid development of deep learning techniques, deep neural network based methods have demonstrated impressive performance in various remote sensing applications such as scene classification Guo et al. [2024], Yang et al. [2022], semantic segmentation Zhao et al. [2024], geological interpretation Han et al. [2022], image fusion Zhou et al. [2024] and detection Zhang et al. [2023a,b]. However, the increasingly large models pose significant challenges for on-device processing on platforms such as on-orbit satellites. On-device computing is becoming more and more important for some remote sensing applications, e.g., perception processing of remote sensing images on on-orbit satellites and unmanned aerial vehicles (UAVs). In these scenarios, two brain-like capabilities are desired for remote sensing models, 1) *high energy efficiency*, allowing the model to operate on edge devices with limited computing resource such as on-orbit satellites and UAVs, 2) *online adaptation*, enabling the model to fast adapt to environmental variations, weather changes and sensor drifts.

The human brain, as the most complex and mysterious natural information processing system in the world, is an ultra complex neuron system with about 100 billion neurons and more than 1000 trillion synapse connections Zhang [2019].

* Brain-Inspired Application Technology Center (BATC), School of Electronic Information and Electrical Engineering, Shanghai Jiao Tong University, Shanghai, China, 200240.

[†] Corresponding Author: wenfei@sjtu.edu.cn

However, the human brain only consumes about 20 wattsSengupta and Stemmler [2014], which is several orders of magnitude more energy efficient than modern computers. The human brain works in an ultra efficient event-driven way, by using spikes to encode and transmit information between neurons. Moreover, the human brain can fast adapt to diverse varying environments and has extraordinary online learning ability.

Inspired by the brain, spiking neural networks (SNN) emulates the spiking encoding and processing mechanism to achieve high energy efficiency. Recent years have witnessed significant progress in SNN research Subbulakshmi Radhakrishnan et al. [2021], Kim and Sejnowski [2021], Meng et al. [2023], Li et al. [2021], Yin et al. [2021], Xiao et al. [2022], Fang et al. [2024], Deng et al. [2022], Fang et al. [2023], Wu et al. [2018] with applications in image recognition Zheng et al. [2021], object detection Kim et al. [2020], segmentation Kim et al. [2022], speech recognition Wu et al. [2020], and time-series prediction Mateńczuk et al. [2021]. Recently, some researchers have applied SNN in remote sensing processing. For example, the work Liu et al. [2022a] introduces an approximate derivative algorithm for SNN to extract the spatial-spectral features of HSIs images. The work Liu et al. [2022b] introduces an attention mechanism to realize real-time SNN based classification of HSI images. The work Pang et al. [2024] proposes an efficient SNN transformer for satellite on-orbit computing.

On the other hand, for on-device processing in remote sensing, e.g., on on-orbit satellites and UAVs, it is desired for a pre-trained perception model that can well generalize or fast adapt to environmental variations, weather changes, and/or sensor drift. In the field of remote sensing, there exists a number of recent works that aim to improve the cross-domain performance of deep models. For instance, the works Li et al. [2018] and Xiong et al. [2020] propose novel methods for cross-source image retrieval based on source-invariant deep hashing CNNs and cycle GAN. The work Ma et al. [2021] proposes a strategy based on teacher-ensemble learning and knowledge distillation for cross-source image retrieval. The work Chen et al. [2022] introduces a novel method that uses high-level feature alignment to narrow the difference between the source and target domains at the semantic level. Moreover, in Yan et al. [2019] and Yang et al. [2020], adversarial domain adaptation methods have been proposed for pixel-level classification of very high resolution images and change detection, respectively.

However, the above methods rely heavily on labeled samples or require multiple epochs of training or fine-tuning, making them impractical for real-world deployment on edge devices for fast online adaptation. Meanwhile, as the models becoming larger and larger, the high energy consumption becomes another major issue for deployment on edge devices.

To address the these issues, we propose an efficient online adaptation framework for remote sensing based on brain-inspired SNN. Starting with a pretrained SNN model, we design an efficient, unsupervised online adaptation algorithm. It approximates the backpropagation through time (BPTT) method by partially decoupling the temporal gradient to achieve forward-in-time optimization, which significantly reduces the computational complexity of SNN adaptation learning. Additionally, we introduce an adaptive activation scaling scheme to boost online adaptation performance of SNN, particularly in low time-steps. Furthermore, for the remote sensing detection task, we develop a confidence-based instance weighting scheme, which substantially improves adaptation performance on detection.

The main contributions are summarized as follows.

- 1) We propose an online adaptation framework for SNN based remote sensing. With a pretrained SNN model from ANN-SNN conversion, we design an efficient, unsupervised online adaptation algorithm. It significantly reduces the computational complexity by approximating the BPTT algorithm to achieve forward-in-time optimization in the adaptation learning of the SNN model.
- 2) We design an adaptive activation scaling scheme to dynamically control the activation scale of a SNN model in the adaptation learning procedure, which significantly enhances the adaptation performance, particularly in low time-steps.
- 3) We design a confidence-based instance weighting scheme to significantly improve adaptation performance in the more challenging detection task. This approach selects high-confidence instances for model updating, thereby mitigating the influence of low-confidence instances.
- 4) Extensive evaluation of the proposed method in comparison with representative ANN adaptation methods has been conducted on seven benchmarking datasets, including three classification datasets (RSSCN, WHU-RS19, and AID), two semantic segmentation datasets (DLRSD and WHLDL), and two detection datasets (RSOD and LEVIR). The results demonstrate that the proposed method significantly outperforms existing domain adaptation and domain generalization approaches under varying weather conditions.

While online unsupervised adaptation have been extensively studied for ANN, to our knowledge this work is the first to address the online adaptation of SNN. As presented in this work, extending existing adaptation methods developed for ANN to SNN is not straightforward. To achieve satisfactory adaptation performance for SNN, we have proposed

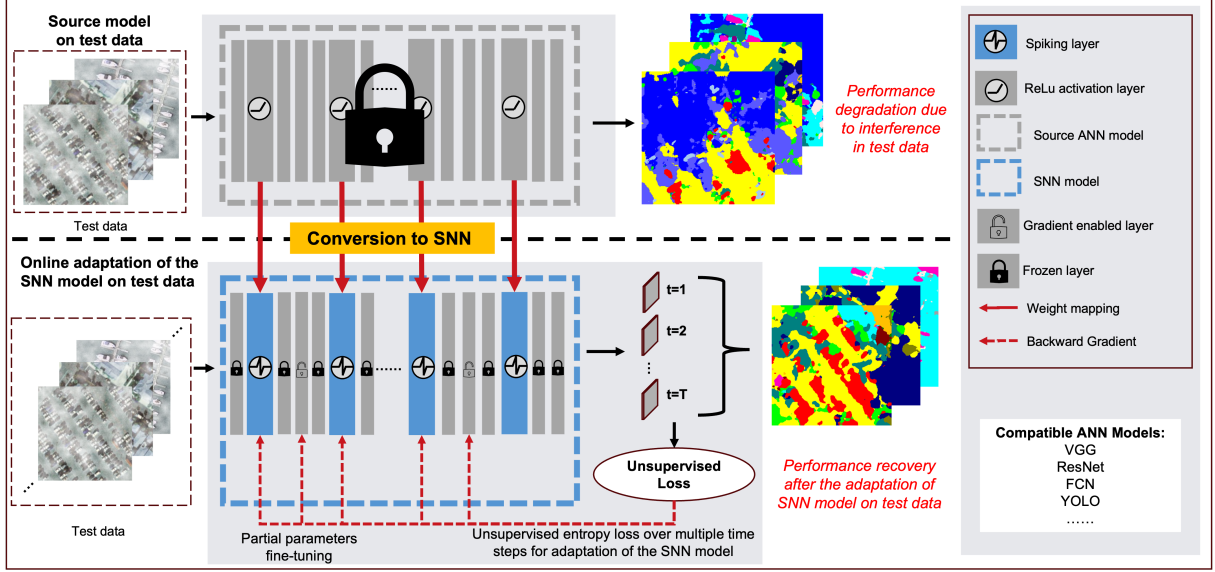


Figure 1: The framework of proposed SNN adaptation pipeline. A pre-trained source model may degrade significantly on test data in wild-world scenarios, e.g., diverse weather conditions. The proposed method adapts a source SNN model on the test data in an online manner based on unsupervised loss, which can significantly improve the SNN model’s performance in such scenarios.

an adaptive activation scaling approach, a confidence-based instance weighting approach. Besides, simplified online SNN optimization algorithm is employed to achieve computationally efficient adaptation. Moreover, to support diverse tasks including classification, segmentation, and detection, this work mainly considers source models from ANN-SNN conversion. However, the proposed method can be straightforwardly applied to directly trained SNN models.

The rest of this paper is organized as follows. Section 2 introduces the detailed components of our proposed SNN adaptation framework. Section 3 introduces the experiment setup, including the datasets and implementation details. Section 4 presents the results and analysis, including experiment results, ablation study, and energy efficiency analysis. Finally, Section 5 provides conclusions and future work.

2 Methodology

The proposed SNN adaptation framework aims to fast adapt to test data with high computational efficiency. In this section, we present its components and implementation details.

2.1 Spiking Neuron Model and Backpropagation Through Time

Drawing inspiration from these biological neural networks, various spiking neuron models have been developed, such as the Hodgkin–Huxley model Abbott [2008], the integrate-and-fire (IF) and leaky integrate-and-fire (LIF) models Hodgkin and Huxley [1952], and the Izhikevich model Izhikevich [2003]. Among them, the IF model simplifies neuron dynamics while preserving essential characteristics and, most importantly, suitable for constructing SNN models from ANN-to-SNN conversion as will be described later. The membrane potential v of an IF model can be expressed as

$$\frac{dv(t)}{dt} = v(t) + X(t), \quad (1)$$

where $X(t)$ is the input current at time t . By accumulating membrane potential over time, the IF neuron fires a spike when the membrane potential reaches a threshold V_{th} , and then is reset by subtracting V_{th} . To facilitate numerical simulation, the dynamic model (1) for a neuron i is typically discretized as

$$\begin{cases} v_i[t+1] = v_i[t] - V_{th} \cdot s_i[t] + \sum_j w_{ij} s_j[t] + b_i, \\ s_i[t+1] = H(v_i[t+1] - V_{th}), \end{cases} \quad (2)$$

where $s_i \in \{0, 1\}$ represents the spike emission, $H(\cdot)$ stands for the Heaviside activation function, w_{ij} denotes the weight between neuron j and neuron i , and b_i is the bias.

Considering the non-differentiable feature of the Heaviside function, to effectively train SNNs by backpropagation, surrogate gradient is widely adopted Neftci et al. [2019], Liu et al. [2022a], Liu et al. [2022b]. Using surrogate gradient, error signals for updating the weights can be propagated by backpropagation through time (BPTT) in both the spatial and temporal directions. For example, consider a multi-layer spiking network with IF neurons as

$$\begin{cases} \mathbf{v}^l[t+1] = \mathbf{v}^l[t] - V_{th} \cdot \mathbf{s}^l[t] + \mathbf{W}^{l-1} \mathbf{s}^{l-1}[t] + \mathbf{b}^l, \\ \mathbf{s}^l[t+1] = H(\mathbf{v}^l[t+1] - V_{th}), \end{cases} \quad (3)$$

where $\mathbf{v}^l \in \mathbb{R}^{n_l}$ collects the membrane potential of n_l neurons in the l -th layer, $\mathbf{s}^l \in \{0, 1\}^{n_l}$ denotes the emitted spikes by the neurons in the l -th layer, $\mathbf{W}^{l-1} \in \mathbb{R}^{n_l \times n_{l-1}}$ stands for the weights connecting the $(l-1)$ -th and l -th layers. Moreover, let \mathcal{L} denote the loss function computed based on the network output over T time-steps. Then, using BPTT to train the network, the gradient of the loss \mathcal{L} with respect to the weights \mathbf{W}^l can be calculated as

$$\frac{\partial \mathcal{L}}{\partial \mathbf{W}^l} = \sum_{t=1}^T \frac{\partial \mathcal{L}}{\partial \mathbf{s}^{l+1}[t]} \frac{\partial \mathbf{s}^{l+1}[t]}{\partial \mathbf{v}^{l+1}[t]} \left(\frac{\partial \mathbf{v}^{l+1}[t]}{\partial \mathbf{W}^l} + \sum_{t' < t} \prod_{k=t-1}^{t'} \left(1 + \frac{\partial \mathbf{v}^{l+1}[k+1]}{\partial \mathbf{s}^{l+1}[k]} \frac{\partial \mathbf{s}^{l+1}[k]}{\partial \mathbf{v}^{l+1}[k]} \right) \frac{\partial \mathbf{v}^{l+1}[t']}{\partial \mathbf{W}^l} \right), \quad (4)$$

where we used $\frac{\partial \mathbf{v}^{l+1}[k+1]}{\partial \mathbf{v}^{l+1}[k]} = 1$ for IF neuron. The non-differentiable term $\frac{\partial \mathbf{s}^{l+1}[t]}{\partial \mathbf{v}^{l+1}[t]}$ is replaced by surrogate functions to approximately compute the backward errors. Recently, surrogate gradient based methods have shown remarkable effectiveness in training SNNs Neftci et al. [2019], Liu et al. [2022a]. Though effective, the computational and memory costs of BPTT scale linearly with the number of time-steps T , as it requires unfolding the the backward computational graph over the T time-steps.

2.2 ANN-SNN Conversion

In this work, we mainly consider pre-trained source models from ANN-SNN conversion, as it facilitates to fully utilize existing ANN models developed for various remote sensing tasks, such as classification, segmentation, and detection. The proposed framework is illustrated in Fig. 1. However, the proposed adaptation method can be straightforwardly applied to directly trained SNN models.

Before proceeding to the proposed online adaptation method, we first briefly introduce ANN-SNN conversion Hu et al. [2023], Wu et al. [2021], Pérez-Carrasco et al. [2013], Han et al. [2020], Bu et al. [2023]. Consider the most widely used activation function ReLU Agarap [2018], the activation of neuron i in layer l can be expressed as

$$a_{l,i} = \max \left(\left(\mathbf{W}_{l-1,i}^{ANN} \right)^\top \mathbf{a}_{l-1} + b_{l,i}^{ANN}, 0 \right), \quad (5)$$

where $^\top$ stands for the transpose operation, $\mathbf{a}_{l-1} \in \mathbb{R}^m$ collects the activation of the m neurons in layer $l-1$, $\mathbf{W}_{l-1,i}^{ANN} \in \mathbb{R}^m$ denotes the weights from the $(l-1)$ -th layer to neuron i in layer l , and $b_{l-1,i}$ denotes the bias of neuron i in layer l . Here, we use the superscript ANN to differentiate between the weights of ANN and that of the converted SNN. By explicitly counting the range of activation values in the l -th layer to determine the maximum activation a_{max}^l , the activation $a_{l,i}$ can be normalized as

$$\bar{a}_{l,i} = \text{clip} \left(\frac{\left(\mathbf{W}_{l-1,i}^{ANN} \right)^\top \mathbf{a}_{l-1}}{a_{max}^l} + \frac{b_{l-1,i}^{ANN}}{a_{max}^l}, 0, 1 \right). \quad (6)$$

For IF neurons, the accumulated voltage $v_{l,i}(T)$ of neuron i in layer l after T time-steps can be expressed as the weighted membrane voltage minus the voltage drop incurred by the spike firing of the previous spiking layer at all times as

$$v_{l,i}(T) = \left(\mathbf{W}_{l-1,i}^{SNN} \right)^\top \sum_t \mathbf{s}_{l-1}(t) + \sum_t b_{l,i}^{SNN} - v_{th} \sum_t s_{l,i}(t), \quad (7)$$

where $\mathbf{W}_{l-1,i}^{SNN} \in \mathbb{R}^m$ denotes the weights connecting from the $(l-1)$ -th layer to neuron i in layer l in the SNN network, $\mathbf{s}_{l-1}(t) \in \mathbb{R}^m$ denotes the spike emission of layer $(l-1)$ at time-step t , $s_{l,i}(t)$ is the spike emission of neuron i in layer l at time-step t , v_{th} is the firing threshold. Rewriting equation (7) as a form of firing rate $r_{l,i}(T) = \frac{\sum_t s_{l,i}(t)}{T}$, it follows that

$$r_{l,i}(T) = \frac{\left(\mathbf{W}_{l-1,i}^{SNN} \right)^\top \sum_t \mathbf{s}_{l-1}(t) + \sum_t b_{l,i}^{SNN}}{T \cdot v_{th}} - \frac{v_{l,i}(T)}{T \cdot v_{th}}. \quad (8)$$

Note that the last term of (8) satisfies that $\frac{v_{l,i}(T)}{T \cdot v_{th}} \ll 1$ since $v_{l,i}(T) < v_{th}$. Hence, it can be ignored for sufficiently large time-steps as

$$r_{l,i}(T) \approx \frac{\left(\mathbf{W}_{l-1,i}^{SNN}\right)^\top \sum_t \mathbf{s}_{l-1}(t) + \sum_t b_{l,i}^{SNN}}{T \cdot v_{th}}. \quad (9)$$

Then, by comparing equation (6) and equation (9), and with $0 \leq r_{l,i}(T) \leq 1$, we can get the mapping between ANN and SNN to convert the weights of an ANN with ReLU activation to an SNN with IF neurons Hu et al. [2023], Wu et al. [2021].

2.3 Adaptive Activation Scaling for Online Adaptation

Given a pre-trained source model, e.g., an SNN model from ANN-SNN conversion as described in the last subsection, our goal is to update the model on test data to improve its performance on the test data. This can be straightforwardly achieved by using an unsupervised loss and a surrogate gradient based algorithm, e.g., the BPTT algorithm introduced in Section II-A or its variants. However, intensive experiments show that, directly updating the SNN model in this way can only achieve a performance far inferior to ANN adaptation methods on cross-domain data.

To bridge the large performance gap between the SNN and ANN adaptation on cross-domain data, we propose an adaptive activation scaling scheme for SNN adaptation to substantially enhance the performance of SNN adaptation. This scheme is designed based on an analysis of the firing rate distribution of a spiking network in adapting on cross-domain data. Figs. 2 shows the distribution (histograms) of the firing rate of different layers in a spiking VGG16 model in cross-domain adaptation. The source domain dataset is RSSCN7, whilst the test data is simulated under cloudy weather condition. Detailed setting is provided in Section 3. From Figs. 2(a) and 2(b), it can be seen that the firing rate distribution of the source model has a shift on the corrupted test data compared to that on the source clean data. This shift in firing rate distribution indicates that, in the presence of domain shift of the test data, the overall firing rate tends to drop and concentrate towards lower values. Similar phenomenon can be observed after the model adaptation on the test data, as shown in Figs. 2(c). The shift of firing rate distribution towards lower values is detrimental to the model's performance. Specifically, it leads to a non-uniformity of the firing rate distribution. For a fixed number T of time-steps, this non-uniformity would significantly degrade the quantization accuracy of spiking representation, and consequently affects the performance of the model. This would be more prominent for a small number of time-steps.

To address this problem, we propose an adaptive activation scaling scheme to adaptively adjust the distribution of firing rate in the adaptation process. Specifically, we consider an additional activation clip parameter for each layer and dynamically adjust it to control the firing rate distribution. The clip parameter is learned in the adaptation process, which is expected to appropriately compress the range of neuron activation and thus mitigate the non-uniformity problem of firing rate.

For a clip parameter α_l for layer l , the neuron activation a_l of layer l is clipped in the feed-forward computation as

$$\bar{a}_l = \max(a_l, \alpha_l) = \begin{cases} \alpha_l, & \text{if } a_l \geq \alpha_l, \\ a_l, & \text{else.} \end{cases} \quad (10)$$

Let $\boldsymbol{\alpha} = [\alpha_1, \dots, \alpha_L]^\top$ collects the clip parameters of all the L layers. As the goal is to appropriately compress the range of neuron activation, we consider a joint loss for optimizing the clip parameters as

$$\min_{\boldsymbol{\alpha}} \mathcal{L}(\boldsymbol{\omega}, \boldsymbol{\alpha}) + \epsilon \|\boldsymbol{\alpha}\|^2, \quad (11)$$

where $\boldsymbol{\omega}$ collects all the parameters of the network other than $\boldsymbol{\alpha}$, \mathcal{L} is the loss function, $\epsilon > 0$ is an ℓ_2 -regularization coefficient. In the formulation (11), the ℓ_2 -regularization is used to decrease the values of $\boldsymbol{\alpha}$. While an excessive decrease of the clip parameters may lead to performance deterioration of the model, the first term $\mathcal{L}(\boldsymbol{\omega}, \boldsymbol{\alpha})$ can help to prevent the performance deterioration. With the formulation (11), in the adaptation process, the clip parameters can be updated together with other model parameters. For example, using SGD, the clip parameter α_l of layer l can be updated as

$$\alpha_l(k+1) = \alpha_l(k) - \eta \left(\epsilon \alpha_l - \eta \frac{\partial \mathcal{L}}{\partial \alpha_l} \right), \quad (12)$$

where η is a learning rate,

Since the firing rate of a spiking neuron can be represented as its activation value divided by the maximum activation of its residing layer, the decrease of α_l is equivalent to the increase of the firing rate of the neurons in the layer. Consequently, using this adaptive activation scaling scheme, we can adjust the range of neuron activation and mitigate the non-uniformity problem of firing rate in the case of data distribution shift. This is verified in Fig. 2(d) that, using

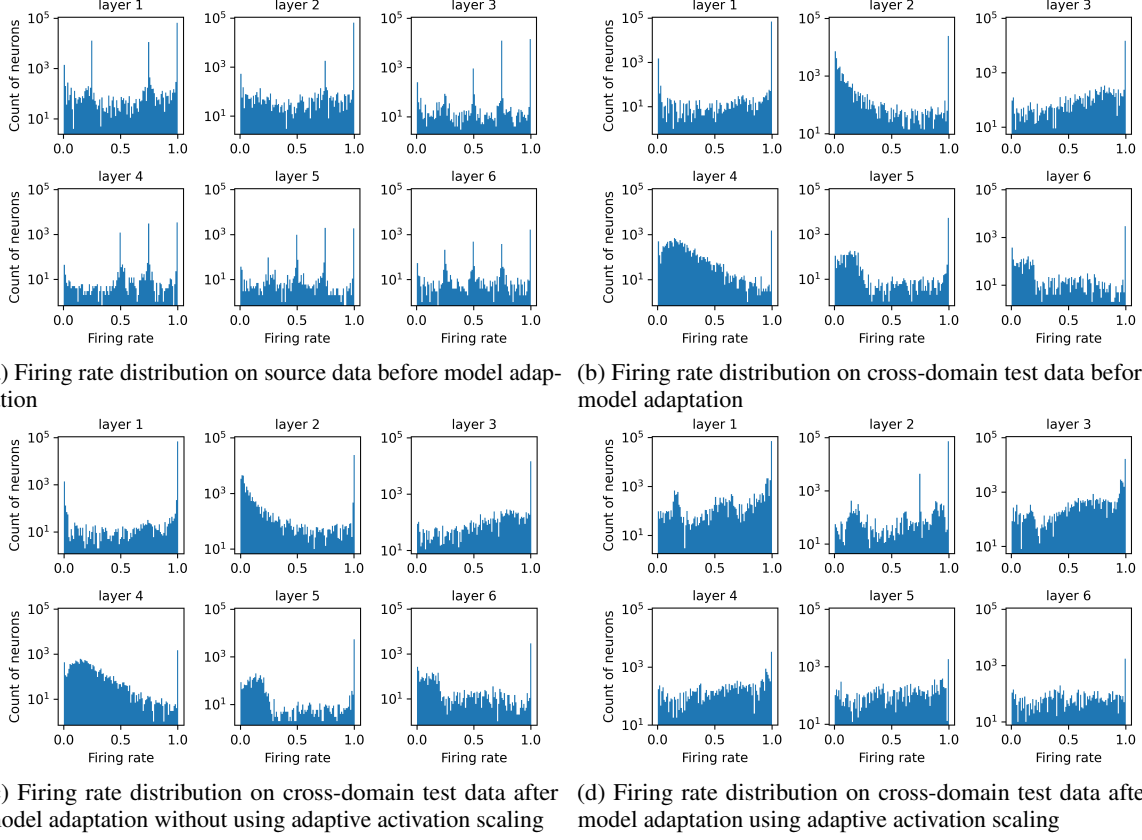


Figure 2: The distribution (histograms) of firing rate of a spiking VGG16 model in cross-domain adaptation. The x-axis represents the firing rate from 0 to 1, and the y-axis (shown in log-scale) represents the count of neurons at each firing rate. The firing rate distribution of the model: (a) on source clean data before model adaptation, (b) on cross-domain test data before model adaptation, (c) on cross-domain test data after model adaptation without using adaptive activation scaling, (d) on cross-domain test data after model adaptation using adaptive activation scaling.

the proposed adaptive activation scaling scheme, the firing rate distribution of a spiking model after adaptation on cross-domain test data becomes more uniform. This would be more prominent for a small number of time-steps.

The proposed mechanism endows an SNN the ability to adjust the firing rate during adaptation, which is crucial for quickly adapting to changing data distributions. As will be shown later in experiments, this mechanism substantially improve the performance of SNN adaptation, especially at low time-steps.

2.4 Unsupervised Online Adaptation Learning for SNN

Consider the applications of real-world on-device adaptation for remote sensing, an adaptation method is expected to be unsupervised without the requirement of labeled data. Meanwhile, the method should be highly-efficient, allowing operation on edge devices with limited computing and memory resources. This section presents an adaptation method to fulfill these two desiderata.

To achieve source-free unsupervised domain adaptation, fully test time domain adaptation (TTA) has recently received much research attention Liang et al. [2020, 2024], Zhao et al. [2023], Sun et al. [2020a], Liu et al. [2021], Wang et al. [2021], Niu et al. [2022], Hong et al. [2023], which enables a pre-trained model to adapt to cross-domain test data in an unsupervised manner. This paper follows the fully TTA works as they are more suitable for on-device processing. Typically, given a pre-trained source model, the model is adapted on unlabeled test samples based on unsupervised losses such as the entropy of the model prediction Wang et al. [2021].

Following these works, we also use the prediction entropy of the model as the objective. Consider the temporal dynamic characteristics of SNN, the network's output is accumulated over multiple time steps. Specifically, for a model with T time-step outputs, let $\mathbf{v}^L[t]$ denote the membrane potential of the last layer (the L -th layer) at time-step t , the final

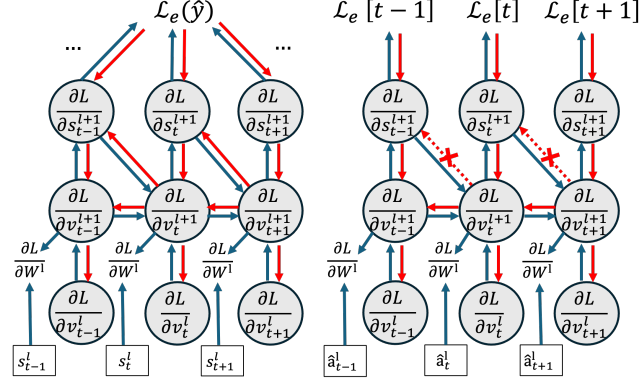


Figure 3: Illustration of the forward and backward computation of (a) BPTT and (b) the approximated online algorithm which can compute the gradient forward-in-time. Backward gradients are drawn in red color.

model prediction is calculated as $\hat{\mathbf{y}} = \frac{1}{T} \sum_{t=1}^T \mathbf{v}^L[t] \in \mathbb{R}^C$, where C is the number of classes for a classification task. With the model prediction $\hat{\mathbf{y}}$, the entropy loss can be written as

$$\mathcal{L}_e(\hat{\mathbf{y}}) = - \sum_c p(\hat{\mathbf{y}}) \log p(\hat{\mathbf{y}}), \quad (13)$$

where $p(\hat{\mathbf{y}}) = \text{softmax}(\hat{\mathbf{y}}) \in \mathbb{R}^C$ stands for the normalized probability expression of the output. Basically, the entropy $\mathcal{L}_e(\hat{\mathbf{y}})$ measures the uncertainty of the model output, of which a smaller value indicates a lower uncertainty.

With the unsupervised entropy loss (13), a gradient based algorithm such BPTT can be used to update the model. However, as mentioned in Section 2.1, using the standard BPTT for an SNN model involves unrolling the network T times along the temporal dimension and requires the maintenance of the computational graph for all previous time steps to backpropagate errors through time. This incurs intensive computational and memory costs that is prohibitive for deployment on edge-devices.

Inspired by the biologically plausible "eligibility traces" mechanism, a highly-efficient credit assignment algorithm for SNN has been proposed in Bellec et al. [2020]. This bio-plausible algorithm integrates the local "eligibility traces" of neurons and global top-down signal to design an efficient credit assignment algorithm for spiking networks that does not require unrolling of the network in time. It only involves forward-in-time computation, and thus substantially reduces the complexity of BPTT, from $O(n^4)$ to $O(n^2)$ for n neurons. More recently, the effectiveness of this method has been demonstrated in deep SNNs Xiao et al. [2022].

Specifically, as illustrated in Fig. 3, this algorithm ignores the term $\frac{\partial \mathbf{v}^{l+1}[k+1]}{\partial \mathbf{s}^{l+1}[k]} \frac{\partial \mathbf{s}^{l+1}[k]}{\partial \mathbf{v}^{l+1}[k]}$ in the full gradient computation of BPTT (4). It is equivalent to partially decouple the computation graph of BPTT in the temporal domain by cutting off the gradient paths $\frac{\partial \mathbf{u}^{l+1}[t+1]}{\partial \mathbf{s}^{l+1}[t]}$, which is corresponding to reset operation of spiking emission on the membrane potential. After partially decoupling the temporal dependencies, an approximated gradient computation of the full BPTT (4) is given by Xiao et al. [2022]:

$$\frac{\partial \mathcal{L}}{\partial \mathbf{W}^l} = \sum_{t=1}^T \frac{\partial \mathcal{L}[t]}{\partial \mathbf{s}^{l+1}[t]} \frac{\partial \mathbf{s}^{l+1}[t]}{\partial \mathbf{v}^{l+1}[t]} \sum_{t' \leq t} \frac{\partial \mathbf{v}^{l+1}[t']}{\partial \mathbf{W}^l}. \quad (14)$$

This simplified algorithm can be implemented without unfolding the network. Specifically, in implementation, it only needs to track the presynaptic activities for each neuron in forward-in-time computation as $\hat{\mathbf{a}}^l[t+1] = \hat{\mathbf{a}}^l[t] + \mathbf{s}^l[t+1] = \sum_{t' \leq t} \mathbf{s}^l[t']$. Then, denote $\mathbf{g}_{\mathbf{v}^{l+1}}[t] = \frac{\partial \mathcal{L}(t)}{\partial \mathbf{s}^{l+1}[t]} \frac{\partial \mathbf{s}^{l+1}[t]}{\partial \mathbf{v}^{l+1}[t]}$ which dose not contain temporal dependencies, the gradient of $\mathcal{L}(t)$ with respect to \mathbf{W}^l , denoted by $\nabla_{\mathbf{W}^l} \mathcal{L}[t]$, can be computed at each time step independently as $\nabla_{\mathbf{W}^l} \mathcal{L}[t] = (\mathbf{g}_{\mathbf{v}^{l+1}}[t])^\top \hat{\mathbf{a}}^l[t]^\top$. Therefore, the gradient can be computed in a forward-in-time manner without unrolling the network, which substantially reduces the computation and memory load. In comparison, for a time-step T , the BPTT algorithm requires unrolling of the network T times, of which the memory cost increases linearly with the time-step number T .

In this algorithm, instantaneous loss $\mathcal{L}(t)$ is used. To apply the unsupervised entropy loss to this online algorithm, we define instantaneous entropy loss for each time-step as

$$\mathcal{L}_e[t] = - \sum_c p(\mathbf{v}^L[t]) \log p(\mathbf{v}^L[t]), \quad (15)$$

where $p(\mathbf{v}^L[t]) = \text{softmax}(\mathbf{v}^L[t]) \in \mathbb{R}^C$, $\mathbf{v}^L[t]$ denotes the membrane potential of the last layer (the L -th layer) at time-step t .

In this way, instantaneous entropy loss is defined at each time-step, which does not require accumulation across time steps. It is used to generate an unsupervised error signal at each time step, enabling the SNN model to perform unsupervised online adaptation learning. As shown in Fig. 3, this algorithm in fact approximates BPTT with gradients be calculated instantaneously at each time step to update the weights. By this means, it does not require maintaining the unfolded computational graph in the temporal dimension and only requires constant memory cost agnostic to time steps.

Moreover, extensive experimental studies show that, when using an SNN model converted from an ANN model that is trained by backpropagation rather than the approximated online training algorithm, using a proper temperature parameter in calculating the model prediction benefits the entropy minimization based model adaptation. With a temperature scaling, the model prediction can be expressed as

$$p(\mathbf{v}^L[t]) = \text{softmax}\left(\frac{\mathbf{v}^L[t]}{\tau}\right), \quad (16)$$

where τ is a temperature coefficient, which smooths the prediction probability.

2.5 Confidence Based Instance Weighting for the Detection Task

To adapt a detection model on unlabeled test data is more challenging than that in the classification and segmentation tasks. Intensive experiment studies show that, directly applying the entropy minimization based method to adapt a detection model can even yield worse performance than the feed-forward only BN method, as will be shown later in TABLE 6. In this section we propose a confidence based instance weighting scheme to significantly improve the adaptation performance on the detection task.

As this work considers on-device perception processing for remote sensing, we mainly focus on one-stage detection models, e.g. YOLO Zhang et al. [2024], Shi et al. [2024], which are more efficient than two-stage models and hence more suitable for on-device deployment. Unlike the classification and semantic segmentation tasks, the detection task poses unique challenges as it involves additional bounding box regression and filtering of redundant predicted boxes. Mainstream detection models typically generate a large number of bounding box predictions, many of which may be low-quality or false positives, necessitating post-processing procedures like non-maximum suppression to eliminate low-quality or redundant boxes. Accordingly, in frameworks like YOLO, a large number of predictions are often filtered out. Therefore, for adapting an one-stage detection model, directly applying classification entropy minimization to all the predicted instances without selection cannot achieve satisfactory performance and may even be detrimental to the performance.

The rationale behind the proposed method is explained as follows. Typically, a detection model generates a large number of predicted instances, in which a large portion are noisy and unreliable, we design a confidence-based weighting scheme that filters out low-confidence ones in the predicted instances, and selectively use high-confidence instances to compute entropy loss for adaptation. Specifically, we design a weighting function based on the confidence scores produced by the detection head of a one-stage model to assign weights for the predicted instances in calculating the entropy loss. For a test image sample, denote $\mathbf{P}_{cf} \in \mathbb{R}^{H \times W}$ as the confidence score output by the detection head, where H and W denote the feature map size of the last layer of the detection head. \mathbf{P}_{cf} contains the confidence score of the presence of an object at each feature in the $H \times W$ feature map, and \mathbf{P}_{cl} contains the corresponding class prediction on C classes at each feature. Then, based on the confidence scores, a weighting function ω is calculated as

$$\omega(\mathbf{P}_{cf}) = \frac{1}{1 + e^{\delta(\mathbf{P}_{cf} - \tau_1)}} + \frac{1}{1 + e^{-\delta(\mathbf{P}_{cf} - \tau_2)}}, \quad (17)$$

where τ_1 and τ_2 specify the boundaries that distinguishes between high confidence and low confidence. The parameter δ controls the steepness of the weighting function. In this weighting function, given a confidence score $\mathbf{P}_{cf}(i, j)$ of the (i, j) -th feature of the last feature map, it is considered to be of low confidence if $\tau_1 < \mathbf{P}_{cf}(i, j) < \tau_2$, otherwise it is considered to be of high confidence. Intuitively, $\mathbf{P}_{cf}(i, j) < \tau_1$ indicates a high confidence of no object, while $\mathbf{P}_{cf}(i, j) > \tau_2$ indicates a high confidence of the presence of an object. Therefore, formula (17) assigns low weight for $\tau_1 < \mathbf{P}_{cf}(i, j) < \tau_2$ to filter out low-confidence instances.

With the weighting function (17), we define an instantaneous entropy loss for online optimizing the detection model as

$$\mathcal{L}_e[t] = - \sum_{i=1}^H \sum_{j=1}^W \sum_{c=1}^C \omega(\mathbf{P}_{cf}(i, j)) \cdot \mathbf{P}_{cl}(i, j, c) \log \mathbf{P}_{cl}(i, j, c), \quad (18)$$

where $\mathbf{P}_{cl} \in \mathbb{R}^{H \times W \times C}$ contains the multi-class predictions by the detection head at each feature of the last feature map. This approach optimizes the model only based on high-confidence instances, which can mitigate influence of low-confidence instances. As will be shown in experiments, this approach can substantially improve the performance of adapting a detection model.

2.6 Framework of the Proposed Online Adaptation Method

The proposed online adaptation method aims to updates a pre-trained model on-the-fly in the on-device testing phase. This subsection provides a holistic overview of it. Given a source SNN model for remote sensing image classification, semantic segmentation or detection, e.g. from ANN-SNN conversion, we update the model parameters on test data in a online streaming manner. More specifically, upon receiving a batch of input test data, the model produces predictions on this batch and, at meantime, updates its parameters based on the unsupervised instantaneous entropy losses (15) and (18). In this manner, the pipeline updates the model on-the-fly.

In the online adaptation phase, only a small portion of the model parameters are updated. In the experiments, we only update the normalization layers, which is sufficient for achieving satisfactory performance in adapting to corruptions arise in the considered cross-domain remote sensing scenarios. Besides, in the online adaptation phase, the adaptive activation scaling scheme proposed in Section 2.3 is adopted to adaptively adjust the firing rate distribution, which introduces additional clip parameters to be learned in the adaptation phase. Overall, the parameters to be updated online include the parameters in normalization layers and the clip parameters. For a BN normalization layer, it typically first centers and standardizes the input x as $\bar{x} = (x - \mu)/\sigma$, where μ and σ denote the mean and standard deviation, respectively. Then it uses an affine transformation $x' = \gamma\bar{x} + \beta$ to transform \bar{x} with affine parameters γ and β for scale and shift, respectively. In the online adaptation phase, only the affine parameters $\{\gamma, \beta\}$ of the normalization layers and the clip parameters $\{\alpha_l\}$ are updated, which account for only a very small fraction of the model. This benefits the adaptation efficiency.

The proposed framework is compatible with most deep learning models, such as VGG, ResNet, WideResNet, FCN, and other mainstream models. Moreover, it is applicable to various tasks, such as the classification, semantic segmentation and detection tasks as considered in the experiments of this work.

3 Experimental Setup

This section introduces the datasets, the synthesis method to generate corrupted data to simulate real-world domain shifts in remote sensing, and the details of experiment settings.

3.1 Datasets

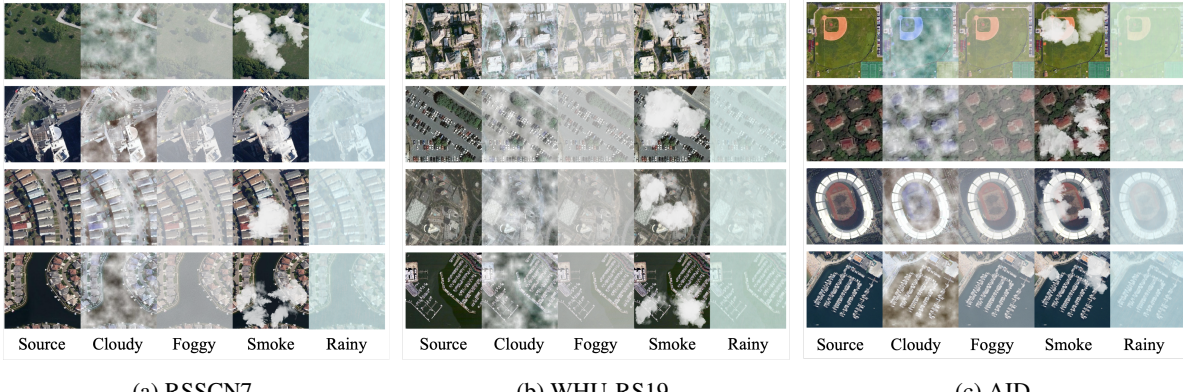
To comprehensively evaluate the performance of the proposed method, we consider three remote sensing image processing tasks, including classification, semantic segmentation and detection tasks. For the classification task, we use the RSSCN7 Zou et al. [2015], WHU-RS19Dai and Yang [2010], and AIDXia et al. [2017] datasets. For the semantic segmentation task, we use the WHDLD Shao et al. [2018], Shao et al. [2020] and DLRSDShao et al. [2018], Chaudhuri et al. [2017] datasets. For the detection task, we use the RSOD and LEVIR datasets. Detailed information about these seven datasets are provided in Table 1.

3.2 Method for Synthesizing Corrupted Data in Remote Sensing Scenarios

Due to the difficulty in collecting real-word datasets under different environmental variations and weather changes, and the lack of open-source datasets, we use widely accepted synthesis methods in the field of remote sensing image processing to generate corrupted data for experimental evaluation. To realistically simulate real-world data domain shift scenarios in remote sensing, we consider four typical weather conditions in synthesizing data corruption, which are cloudy, foggy, smoke, and rainy weather conditions.

Table 1: Details of the seven datasets used in experiments for the three tasks.

Task	Dataset	Classes	Resolution	Source	Size	Number of images/targets
Classification	RSSCN7	7	-	Google Earth	400*400	2800
	WHU-RS19	19	0.5	Google Earth	600*600	1005
	AID	30	0.5-8	Google Earth	600*600	10000
Semantic segmentation	WHDLD	6	2.0	UCMerced USGS National Map	256*256	4940
	DLRSD	17	2.0		256*256	2100
Detection	RSOD	4	0.3-3.0	Google Earth	1044*915	6950
	LEVIR	3	0.2-1.0	Google Earth	800*600	11028



(a) RSSCN7

(b) WHU-RS19

(c) AID

Figure 4: Examples of source clean images and their corrupted versions under four types of weather conditions for each dataset. (a) The RSSCN7 dataset. (b) The WHU-RS19 dataset. (c) The AID dataset

For cloudy condition, we generate synthetic cloudy image I_c by summing multi-scale random noise images Sun et al. [2021]. The synthesis process can be expressed as

$$I_c = \sum_s \Psi(Rand(2^s)) / 2^s, \quad (19)$$

where $Rand(2^s)$ denotes a randomizing function that produces random noise with an image size of 2^s , and Ψ denotes the operator that resizes the random noise to the cloud image size. The scale factor s is a natural number ranging from 1 to $\log_2(N)$, where N is the cloudy image size.

For the foggy condition, we use the diamond-square algorithm to render the fog Shi et al. [2022]. As for the smoke and rainy environments, we use the Adverse-Weather-Simulation to render images Yang [2023]. Example samples of source images and rendered synthetic corrupted images with different weather conditions are shown in Figs. 4.

3.3 Implementation Detail and Experimental Settings

In the experiments, we consider VGG16 Simonyan and Zisserman [2014] and ResNet34 He et al. [2016] as the backbone networks for the classification task, the classic FCN Long et al. [2015] network as the backbone network for the semantic segmentation task, and classic YOLOv3 Redmon and Farhadi [2018] with Darknet backbone as the detection network.

First, we randomly split the clean source datasets into training and testing sets by 80% and 20% for each category, and then render the testing sets into corrupted testing sets using the above synthesis methods. After training the networks on the clean source training sets, we test them with the clean source testing sets to verify that the networks perform well on the source data. We then convert these ANN models into SNN as introduced in Section 2.2, and configure them to update the forward and backward propagation parameters of specific layers, as described in Section 2.6. This process does not involve additional training or learning.

During adaptation, we feed the synthesized corrupted testing data to the SNN model. Since our method does not require source domain data, it is source-free. Meanwhile, it updates the affine parameters of the normalization layers and the

Table 2: Results of the compared adaptation methods in the classification task on the RSSCN7 dataset. Top-1 accuracy (%) is reported.

Model	Method	Model type	Source	Target	Loss	Cloudy	Foggy	Smoke	Rainy	Mean Acc
VGG16	Oracle	ANN	\times	x^t	-	-	-	-	-	96.54
	Source-only	ANN	\times	x^t	-	27.32	43.39	30.89	36.25	34.46
	TTTSun et al. [2020b]	ANN	x^s, y^s	x^t	$L(x^s, y^s) + L(x^s)$	52.56	63.52	54.58	58.45	57.28
	ADAGanin and Lempitsky [2015]	ANN	x^s, y^s	x^t	$L(x^s, y^s) + L(x^s, x^t)$	51.56	61.71	52.18	57.76	55.80
	BNSchneider et al. [2020]	ANN	\times	x^t	-	53.54	68.26	60.58	65.85	62.06
	TentWang et al. [2020]	ANN	\times	x^t	$L(x^t)$	68.52	72.58	62.08	72.58	68.94
ResNet34	Ours	SNN	\times	x^t	$L(x^t)$	69.25	73.05	64.75	73.06	70.03
	Oracle	ANN	\times	x^t	-	-	-	-	-	97.35
	Source-only	ANN	\times	x^t	-	37.32	46.25	36.79	47.68	42.01
	TTTSun et al. [2020b]	ANN	x^s, y^s	x^t	$L(x^s, y^s) + L(x^s)$	53.78	64.58	55.87	59.54	58.44
	ADAGanin and Lempitsky [2015]	ANN	x^s, y^s	x^t	$L(x^s, y^s) + L(x^s, x^t)$	52.58	63.47	55.25	58.58	57.47
	BNSchneider et al. [2020]	ANN	\times	x^t	-	62.57	70.46	61.92	69.52	66.12
	TentWang et al. [2020]	ANN	\times	x^t	$L(x^t)$	68.28	75.25	64.14	72.58	70.06
	Ours	SNN	\times	x^t	$L(x^t)$	71.06	75.55	65.05	74.25	71.48

adaptive activation scaling parameters based on unsupervised entropy loss. Additionally, as the model processes on and adapts to each batch of test data in a streaming manner, updating parameters immediately after each batch input, our method is fully online and operates on-the-fly.

The experiments are implemented using the Pytorch library. All experiments are conducted on an NVIDIA GeForce RTX4090 GPU with 24G graphics memory.

4 Results and Analysis

4.1 Compared Methods and Evaluation Metrics

To comprehensively evaluate the proposed method in comparison with existing methods, the following state-of-the-art unsupervised adaptation methods are compared.

1. *Oracle*: Oracle means a model is only trained on the labeled source domain training data while tested on source domain testing data. Since test samples are clean and independently identically distributed with the source domain training samples, the oracle model provides a upper bound of performance.
2. *Source-only*: Source-only represents a pre-trained source model is directly tested on the corrupted data without adaptation. Its performance would drop dramatically since the model does not adapt to the test data with domain shift. It provides a lower bound of performance and helps reflect the effectiveness of the adaptation methods.
3. *TTT*: Test-time training (TTT)Sun et al. [2020b] trains a model based on joint supervised and self-supervised tasks on source domain, and then uses the self-supervised task to train the model on test data.
4. *ADA*: The adversarial domain adaptation (ADA) method Ganin and Lempitsky [2015] reverses the gradients of a domain classifier on source and test data to learn domain-invariant representation.
5. *AdaptSegNet*: AdaptSegNet Tsai et al. [2018] first adopts adversarial learning in the output space for UDA semantic segmentation. Compared with adaptation at the feature level, the structured output spaces of the source and target domains contain global context and spatial similarities, which are beneficial for adaptation. In this method, a multilevel adversarial network is designed to enhance the model.
6. *ADVENT*: Building on AdaptSegNet, ADVENT Vu et al. [2019] calculates the entropy of the output space to avoid low-confidence predictions in the target domain. The entropy map is then fed into the discriminator for adversarial training.
7. *BN*: It only updates the normalization statistics Schneider et al. [2020] on test data during testing, which only involves froward computation.
8. *Tent*: Test entropy (Tent) Wang et al. [2020] adapts a model on test data by minimizing the entropy of the model prediction.

We exclusively evaluate TTT and ADA for the classification task, while AdaptSegNet and ADVENT are exclusively evaluated for the semantic segmentation task. BN and Tent are evaluated for all the three tasks. Compared to the

Table 3: Results of the compared adaptation methods in the classification task on the WHU-RS19 dataset. Top-1 accuracy (%) is reported.

Model	Method	Model type	Source	Target	Loss	Cloudy	Foggy	Smoke	Rainy	Mean Acc
VGG16	Oracle	ANN	\times	x^t	-	-	-	-	-	92.54
	Source-only	ANN	\times	x^t	-	32.45	42.75	31.80	47.55	38.64
	TTTSun et al. [2020b]	ANN	x^s, y^s	x^t	$L(x^s, y^s) + L(x^s)$	49.65	55.71	48.32	57.43	52.78
	ADAGanin and Lempitsky [2015]	ANN	x^s, y^s	x^t	$L(x^s, y^s) + L(x^s, x^t)$	47.25	53.48	47.57	56.38	51.17
	BNSchneider et al. [2020]	ANN	\times	x^t	-	51.35	54.62	52.83	63.15	55.49
	TentWang et al. [2020]	ANN	\times	x^t	$L(x^t)$	54.28	59.54	56.08	64.58	58.62
ResNet34	Ours	SNN	\times	x^t	$L(x^t)$	55.86	59.57	57.04	64.78	59.31
	Oracle	ANN	\times	x^t	-	-	-	-	-	96.35
	Source-only	ANN	\times	x^t	-	33.83	43.60	32.34	48.26	39.51
	TTTSun et al. [2020b]	ANN	x^s, y^s	x^t	$L(x^s, y^s) + L(x^s)$	51.79	54.48	49.67	59.67	53.90
	ADAGanin and Lempitsky [2015]	ANN	x^s, y^s	x^t	$L(x^s, y^s) + L(x^s, x^t)$	48.35	53.85	48.46	59.58	52.56
	BNSchneider et al. [2020]	ANN	\times	x^t	-	52.76	55.73	53.94	64.25	56.67
ResNet34	TentWang et al. [2020]	ANN	\times	x^t	$L(x^t)$	55.78	59.13	56.63	65.20	59.19
	Ours	SNN	\times	x^t	$L(x^t)$	56.67	59.54	56.68	65.36	59.56

Table 4: Results of the compared adaptation methods in the classification task on the AID dataset. Top-1 accuracy (%) is reported.

Model	Method	Model type	Source	Target	Loss	Cloudy	Foggy	Smoke	Rainy	Mean Acc
VGG16	Oracle	ANN	\times	x^t	-	-	-	-	-	91.85
	Source-only	ANN	\times	x^t	-	14.25	21.85	16.70	18.45	17.81
	TTTSun et al. [2020b]	ANN	x^s, y^s	x^t	$L(x^s, y^s) + L(x^s)$	34.89	49.50	39.52	40.64	41.14
	ADAGanin and Lempitsky [2015]	ANN	x^s, y^s	x^t	$L(x^s, y^s) + L(x^s, x^t)$	34.15	45.68	37.86	39.57	39.32
	BNSchneider et al. [2020]	ANN	\times	x^t	-	37.64	53.19	40.19	44.95	43.99
	TentWang et al. [2020]	ANN	\times	x^t	$L(x^t)$	42.67	55.68	41.67	51.58	47.90
ResNet34	Ours	SNN	\times	x^t	$L(x^t)$	43.37	55.84	41.99	52.57	48.44
	Oracle	ANN	\times	x^t	-	-	-	-	-	92.15
	Source-only	ANN	\times	x^t	-	13.45	22.75	15.80	19.55	17.89
	TTTSun et al. [2020b]	ANN	x^s, y^s	x^t	$L(x^s, y^s) + L(x^s)$	34.99	49.60	39.96	39.67	41.06
	ADAGanin and Lempitsky [2015]	ANN	x^s, y^s	x^t	$L(x^s, y^s) + L(x^s, x^t)$	34.25	44.78	38.62	39.74	39.35
	BNSchneider et al. [2020]	ANN	\times	x^t	-	35.54	51.09	40.81	42.85	42.57
ResNet34	TentWang et al. [2020]	ANN	\times	x^t	$L(x^t)$	42.57	56.53	41.89	52.18	48.29
	Ours	SNN	\times	x^t	$L(x^t)$	43.27	56.74	42.56	52.47	48.76

classification and segmentation tasks, the research on online adaptation for the detection task is very limited VS et al. [2023]. In the experiment on the detection task, we apply the BN and Tent methods Schneider et al. [2020], Wang et al. [2020] to the detection task, and compare them with the proposed method. It is also important to acknowledge that some methods deviate from strictly adhering to fully online settings, unlike our proposed method. Only BN and Tent are compared under exactly the same settings. Other methods may incorporate additional supervision or require access to source data, but our approach still show advantage compared with them.

We use overall accuracy and intersection-over-union (IoU) to evaluate the performance of the methods on the classification task and semantic segmentation task, respectively. For the detection task, the performance of the methods are evaluated in terms of mean average precision (mAP).

4.2 Results on the Classification Task

TABLE 2 presents the classification accuracy of the compared methods on the RSSCN7 dataset. For a fair comparison, all methods use the same backbone model. We consider two backbones, VGG16 and ResNet34. We report the accuracy on corrupted data in the cloudy, foggy, smoke, and rainy conditions, and present the mean overall accuracy across these four conditions. Before adaptation, both the VGG and ResNet models can achieve a high accuracy (96.54% and 97.35%, respectively) on the clean source data. However, both models experience a large accuracy drop of more than 50% on corrupted data, indicating that weather interference can lead to significant deterioration of the models' performance. It can be seen that, TTT and ADA can improve the performance by over 20% but they additionally use source data.

BN and Tent can raise the accuracy to over 60%, e.g., reaching 62.06% and 68.94% with the VGG16 network, and 66.12% and 70.06% with the ResNet34 network, respectively. While BN only updates the normalization layers' statistics parameters during forward computation, Tent additionally updates the affine parameters of the normalization layers through backpropagation, which has better adaptation performance than BN. Our method using an SNN model

Table 5: Results of the compared adaptation methods in the semantic segmentation task on the DLRSD and WHDLD datasets. Mean intersection-over-union (mIoU) (in %) is reported.

Dataset	Method	Model type	Source	Target	Loss	Cloudy	Foggy	Smoke	Rainy	Mean mIoU
DLRSD	Oracle	ANN	\times	x^t	-	-	-	-	-	66.05
	Source-only	ANN	\times	x^t	-	17.25	31.75	15.75	35.75	25.13
	AdaptSegNetTsai et al. [2018]	ANN	x^s, y^s	x^t	$L(x^s, y^s) + L(x^s, x^t)$	19.78	40.72	20.85	41.52	30.72
	ADVENTVu et al. [2019]	ANN	x^s, y^s	x^t	$L(x^s, y^s) + L(x^s, x^t) + L(x^t)$	21.86	42.18	23.48	42.85	32.59
	BNSchneider et al. [2020]	ANN	\times	x^t	-	27.42	43.79	28.85	46.72	36.70
	TentWang et al. [2020]	ANN	\times	x^t	$L(x^t)$	33.15	47.78	32.87	48.27	40.52
WHDLD	Ours	SNN	\times	x^t	$L(x^t)$	34.35	47.88	33.72	49.16	41.28
	Oracle	ANN	\times	x^t	-	-	-	-	-	64.38
	Source-only	ANN	\times	x^t	-	19.17	29.89	14.06	31.67	23.70
	AdaptSegNetTsai et al. [2018]	ANN	x^s, y^s	x^t	$L(x^s, y^s) + L(x^s, x^t)$	22.48	38.28	25.85	42.04	32.16
	ADVENTVu et al. [2019]	ANN	x^s, y^s	x^t	$L(x^s, y^s) + L(x^s, x^t) + L(x^t)$	34.82	40.06	28.95	43.28	36.78
	BNSchneider et al. [2020]	ANN	\times	x^t	-	39.74	45.79	33.87	51.85	42.81
WHDLD	TentWang et al. [2020]	ANN	\times	x^t	$L(x^t)$	41.22	47.32	35.92	53.57	44.51
	Ours	SNN	\times	x^t	$L(x^t)$	42.38	48.06	36.28	54.09	45.20

achieves the best performance in terms of mean accuracy with both VGG16 and Resnet34 backbones, e.g., 70.03% and 71.48%, respectively.

TABLE 3 shows the results on the WHU-RS19 dataset. On the WHU-RS19 dataset, the source models without adaptation also drop over 50% of accuracy from the oracle. The TTT method slightly outperforms ADA, while Tent slightly outperforms BN. The proposed method again achieves the best performance, e.g., 59.31% and 59.56% accuracy with the VGG16 and ResNet34 backbones, respectively. On the AID dataset, we observe a similar trend from TABLE 4. Due to the increase of classes and the complexity of the image data, the source models drop more compared to their performance on the other two datasets. While the source models achieve over 91% accuracy on the source data, they only have an accuracy less than 20% on corruption data, indicating that the models fail in challenging scenarios when facing corruption. As shown in TABLE 4, with the VGG16 backbone, the TTT and ADA methods yield accuracy around 40%, whilst BN and Tent have better performance reaching 43.99% and 47.9%, respectively. Our method achieves an accuracy over 48% with both backbones. From the results, we can observe that the overall accuracy on cloudy and smoke corruptions is lower than that on the other two corruptions. This is due to the nature that the cloudy and smoke conditions are more challenging, in which the corruption obscures the original features and significantly increases the difficulty for adaptation. But overall, our SNN adaptation method shows strong adaptation capability and outperforms the compared adaptation methods.

4.3 Results on the Semantic Segmentation Task

To demonstrate the broad applicability of the proposed method, we further conduct adaptation experiments on semantic segmentation of remote sensing images. We use FCN Long et al. [2015] as the backbone network and conduct adaptation experiments on two optical remote sensing datasets, WHDLD Shao et al. [2018, 2020] and DLRSD Shao et al. [2018], Chaudhuri et al. [2017]. TABLE 5 shows the semantic segmentation performance of the compared methods on the WHDLD and DLRSD datasets.

It can be seen from TABLE 5 that, weather interference has a significant negative impact on the performance of segmentation models. The backbone network, which is well-trained on the source domain with over 60% mIoU, degrades to have an mIoU barely above 20% on corrupted test data. The degradation is especially conspicuous under the cloudy and smoke conditions. On the DLRSD dataset, the source-only method achieves only 17.25% and 15.75% mIoU under the cloudy and smoke conditions, respectively. Similar large degradation of the source model can also be observed on the WHDLD dataset, e.g., with an mIoU of 19.17% and 14.06% on the cloudy and smoke conditions, respectively.

The AdaptSegNet and ADVENT methods leverage adversarial training between the source and target domain data to enhance the generalization capability. On the two datasets, AdaptSegNet achieves 30.72% and 32.16% mIoU, while ADVENT reaches 32.59% and 36.78% mIoU, respectively. BN and Tent can further improve the adaptation performance to 36.7% and 40.52% on the DLRSD dataset, and to 42.81% and 44.51% on the WHDLD dataset, respectively. BN and Tent do not require access to the source domain data, highlighting their significant advantage in source-free adaptation scenarios. Our method shows the best adaptation performance, achieving mIoU of 41.28% and 45.20% on the DLRSD and WHDLD datasets, respectively, surpassing all other compared methods. Figs. 5 visualizes segmented results on samples from the WHDLD dataset by the proposed method in comparison with the source model.

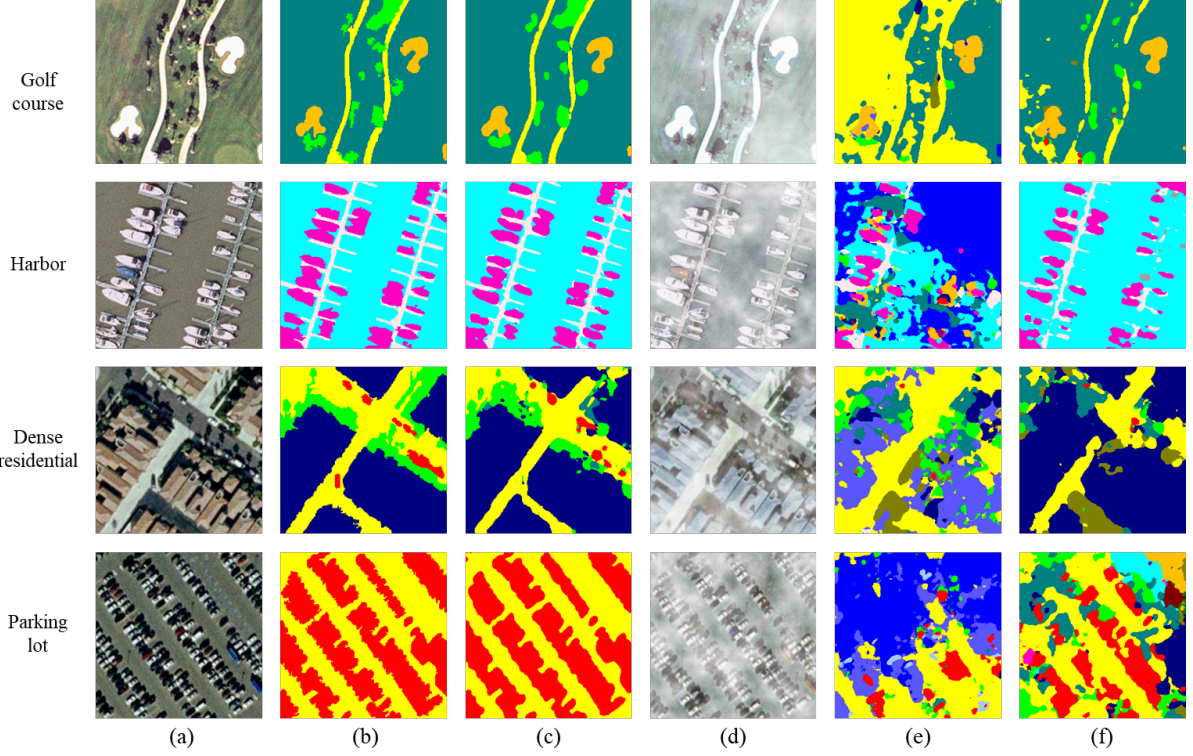


Figure 5: Visualization of segmented results on image samples from the WHLDL dataset by the compared methods. (a) Original images. (b) Ground-truth segmentation. (c) Oracle. (d) Cloudy images. (e) Source-only model. (f) Our method.

Table 6: Results of the compared adaptation methods in the detection task on the RSOD and LEVIR datasets. mAP (in %) is reported.

Datasets	Method	Model type	Source	Target	Loss	Cloudy	Foggy	Smoke	Rainy	Mean mAP
RSOD	Oracle	ANN	\times	x^t	-	-	-	-	-	82.71
	Source-only	ANN	\times	x^t	-	12.89	24.92	11.75	26.80	19.09
	BNSchneider et al. [2020]	ANN	\times	x^t	-	39.45	45.24	47.34	48.82	45.21
	TENTWang et al. [2020]	ANN	\times	x^t	$L(x^t)$	39.12	45.15	46.17	47.56	44.50
LEVIR	Ours	SNN	\times	x^t	$L(x^t)$	41.75	46.75	49.85	49.83	47.05
	Oracle	ANN	\times	x^t	-	-	-	-	-	77.84
	Source-only	ANN	\times	x^t	-	11.85	25.76	13.75	23.54	18.73
	BNSchneider et al. [2020]	ANN	\times	x^t	-	35.48	43.82	38.75	45.78	40.96
	TENTWang et al. [2020]	ANN	\times	x^t	$L(x^t)$	34.05	42.76	36.07	44.25	39.28
	Ours	SNN	\times	x^t	$L(x^t)$	37.81	44.25	39.36	47.06	42.12

The results show the impact of weather interference on the performance of the source model and demonstrate the effectiveness of the proposed SNN adaptation method.

4.4 Results on the Detection Task

TABLE 6 shows the detection performance on RSOD and LEVIR datasets. Mean mAP is used to evaluate the overall performance across different weather conditions. As shown in TABLE 6, weather interference significantly impacts the performance of pre-trained detection models. On the RSOD dataset, the mean mAP degrades drastically from 82.71% in the source domain to 19.09% on the corrupted test data. Similarly, on the LEVIR dataset, the mean mAP decreases from 77.84% to 18.73%. This underscores the critical need for effective online adaptation of the pre-trained models when deployed in real-world scenarios to face diverse weather changes.



Figure 6: Visualization of detection results on image samples from the RSOD dataset by the compared adaptation methods under different weather conditions.

However, contrary to the results in previous classification and semantic segmentation experiments, Tent performs worse than BN in the detection task. On the RSOD dataset, Tent’s mAP decreases by 0.71% compared to BN, while on the LEVIR dataset, it decreases by 1.68%. This suggests that calculating the entropy loss based on all the predicted instances without filtering cannot effectively guide the network adaptation. Our proposed strategy, however, utilizes a filtering function to identify high-confidence instances from the detection head outputs, enabling the model to effectively leverage reliable instances for adaptation. On the RSOD dataset, our method improves the mean mAP of the source model from 19.09% to 47.05%. Similarly, on the LEVIR dataset, our method improves the mean mAP from 18.73% to 42.12%. on both the datasets, our method outperforms BN and Tent, achieving the best adaptation performance. Figs. 6 visualizes detected results on image samples from the RSOD dataset by the compared adaptation methods under different weather conditions.

4.5 Ablation Study and Analysis

A series of ablation experiments are conducted to disclose the contributions of each component of the proposed method, including the online algorithm, the adaptive activation scaling scheme, the temperature smooth in (16), and the confidence-based instance weighting approach.

First, we evaluate the effect of the online SNN adaptation algorithm introduced in Section 2.4 in comparison with the full BPTT algorithm introduced in Section 2.1. We conduct an one-epoch adaptation on the RSSCN7 classification dataset, monitoring both accuracy and memory consumption for different times-steps. As shown in Figs. 7, the accuracy of both algorithms increase as the time-step increases, which is expected as SNNs encode information into binary temporal sequences. According to (4), the standard full gradient backpropagation of SNN unrolls the model in the temporal domain, resulting in that the memory consumption increases linearly with the number of time-steps. In comparison, the memory consumption of the online algorithm is constant, which would be more preferred in on-device adaptaiton scenarios.

The second ablation study evaluates the effect of the proposed adaptive activation scaling (AAS) scheme. As introduced in Section (2.3) and Fig. 2, AAS adaptively controls the firing rate distribution of each spiking layer, making the SNN highly flexible during adaptation.

We conduct experiments on the RSSCN7, WHU-RS19, and AID datasets. Figs. 8 shows the adaptation performance of the proposed method with and without the adaptive activation scaling scheme for different time-steps. It can be seen from Figs. 8 that, with small time-steps, the performance of the SNN model is limited.

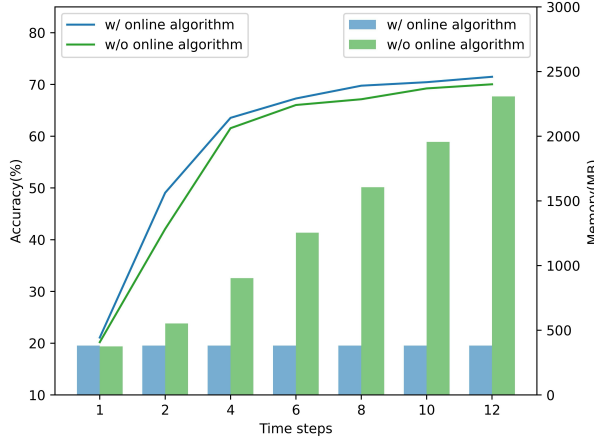


Figure 7: Accuracy and memory consumption of the SNN model during adaptation using BPTT or the online algorithm under different time steps.

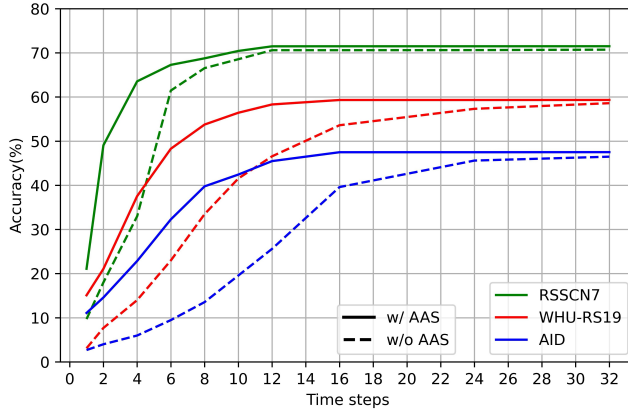


Figure 8: Influence of the proposed adaptive activation scaling (AAS) scheme on the adaptation performance for varying time-steps on different datasets. VGG16 is used as the backbone network.

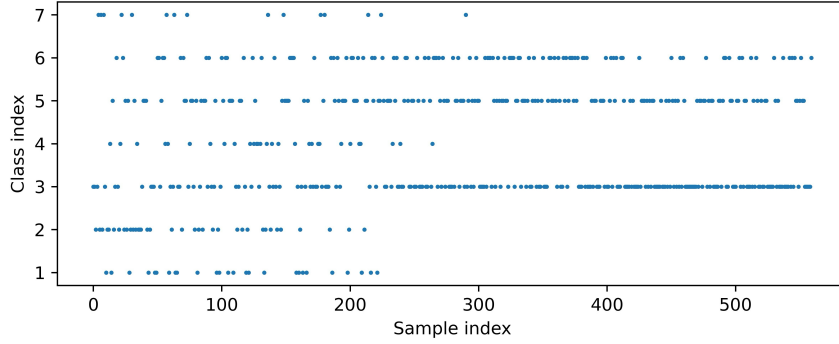
However, under these conditions, using AAS can significantly enhance the model’s adaptation performance. On the RSSCN7 dataset, the adaptation performance improves by over 30% at 4 time-steps. On the WHU-RS19 and AID datasets, the performance increases by 26% and 23% respectively at 6 time-steps. On the whole, the proposed AAS scheme is especially effective at small time-steps. Using smaller time-steps can reduce computational load and the processing latency. Thus, this advantage of the AAS scheme would be particularly preferred in applications, such as on-platform processing with limited computing resources.

The third ablation study examines the effect of the temperature smoothing calculating the instantaneous entropy loss in (15) and (16). TABLE 7 shows the results of proposed method with different values of the temperature parameters using a VGG16 backbone. Three datasets are considered, including the RSSCN7, WHU-RS19 and AID datasets. It can be seen that, without temperature smoothing, the instantaneous entropy loss cannot achieve a satisfactory performance during adaptation. For example, on the RSSCN7 dataset with time-step $T = 4$, without temperature smoothing it only yields an adaptation accuracy of 45.78%, while using a temperature value $\tau = 4$ it yields an adaptation accuracy of 63.54%. On the more complex AID dataset, the contribution of temperature smoothing is even more evident, e.g., the adaptation accuracy of the vanilla entropy loss only reaches about half that of the case with a temperature parameter $\tau = 4$.

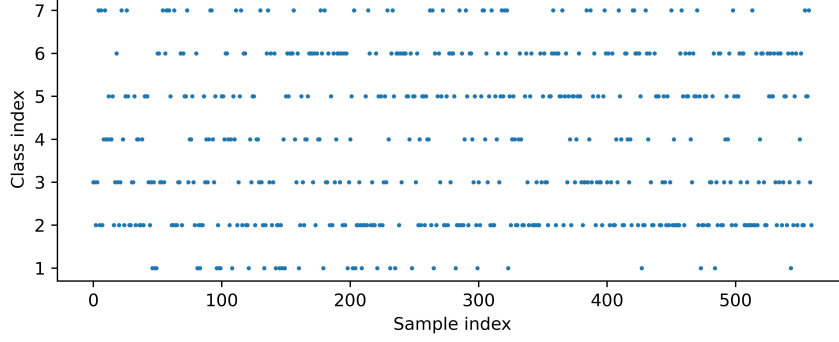
To better analyze the effect of entropy temperature smoothing, we monitor the prediction distribution of the SNN model during one epoch adaptation on the RSSCN7 dataset. As shown in Figs. 9, when using appropriate temperature smoothing, the distribution of model predictions keeps uniform during adaptation as expected since the test samples have a uniform class distribution. In contrast, when using the vanilla entropy loss without temperature smoothing, the predictions tend to abnormally concentrate on a few classes, which is due to model collapse during adaptation.

Table 7: Ablation study on the temperature parameter τ in calculating the instantaneous loss under different numbers of time steps.

Dataset	Temp.	Time-steps					
		2	4	8	12	16	32
RSSCN7	1.0	30.78	45.78	47.96	49.58	51.78	54.82
	2.0	35.28	50.37	53.04	56.29	58.92	60.75
	4.0	49.06	63.54	68.76	71.48	71.5	71.53
	8.0	40.86	55.89	59.24	62.08	63.38	64.93
WHU-RS19	1.0	12.89	28.58	38.85	40.76	41.89	42.85
	2.0	14.15	31.85	47.58	50.78	51.85	53.17
	4.0	21.06	37.54	53.76	58.31	59.34	59.37
	8.0	17.65	34.58	50.48	55.68	56.15	56.82
AID	1.0	9.55	12.25	14.85	20.58	21.75	21.92
	2.0	10.57	13.52	17.57	25.73	26.85	27.97
	4.0	14.58	22.85	39.76	45.48	47.49	47.51
	8.0	10.37	15.25	29.41	36.87	37.85	37.88



(a) Vanilla entropy loss without temperature smoothing



(b) Entropy loss with temperature smoothing

Figure 9: Prediction distribution during adaptation of proposed SNN model. (a) Entropy loss with temperature smoothing ($\tau = 4$). (b) Vanilla entropy loss without temperature smoothing.

Basically, from the physical meaning of entropy, the model can achieve the low entropy objective by constantly generating high-confidence predictions regardless the model inputs. This corresponds to a collapse issue of the entropy minimization loss.

Lastly, we examine the effect of the proposed confidence-based weighting approach on the detection task. As shown in (17) and (18), the parameters τ_1 and τ_2 determine the confidence boundary for high-confidence selection. TABLE 8 shows the results of proposed method with different values of τ_1 and τ_2 on the RSOD dataset. It can be seen that, without using the weighting approach, that is indiscriminately calculating the entropy loss on all the predicted instances,

Table 8: Ablation study on the confidence-based weighting approach with different boundary parameters τ_1 and τ_2 . “w/o CW” denotes the case without using the confidence based weighting approach.

Method	τ_1	τ_2	Cloudy	Foggy	Smoke	Rainy	Mean mAP
BN	-		39.45	45.24	47.34	48.82	45.21
Ours	0.1	0.9	40.87	46.53	48.79	48.98	46.29
	0.2	0.8	41.75	46.75	49.85	49.83	47.05
	0.3	0.7	39.76	46.04	48.42	49.15	45.84
	w/o CW		39.12	45.15	46.17	47.56	44.50

Table 9: Comparison of energy consumption of ANN and SNN for different backbone architectures.

Model	Type	FLOPs (G)	SynOps (G)	Energy (J)
VGG16	ANN	42.39	-	1.70
	SNN ($T=4$)	-	2.27	2.04E-2
ResNet34	ANN	11.63	-	4.65E-1
	SNN ($T=4$)	-	0.56	5.08E-3
FCN	ANN	9.28	-	3.71E-1
	SNN ($T=8$)	-	0.59	5.32E-3

the performance of the proposed adaptation method is even inferior to the simple BN method, with mean mAP 44.5% versus 45.21%.

As the filtering range gradually expands, more low-confidence instances are filtered out, leading to an improvement in adaptation performance. With $\tau_1 = 0.2$ and $\tau_2 = 0.8$, our method achieves the highest mean mAP of 47.05%. However, beyond a certain point, the performance degrades due to the insufficient number of instances available for calculating the entropy loss. For example, with $\tau_1 = 0.1$ and $\tau_2 = 0.9$, the mAP decreases to 46.29%. Overall, with appropriate values of τ_1 and τ_2 , the proposed weighting approach can significantly improve the adaptation performance on the detection task.

4.6 Energy Efficiency Analysis

As the main motivation of this work is to exploit the high energy efficiency of SNN for on-device remote sensing processing, here we provide a comparison on its energy consumption against ANN. We compare the estimated energy consumption of models running on hardware. For ANNs, the computation operations are dominated by floating-point multiply-accumulate computation (MAC), while for SNNs, it only involves accumulate computation (AC) because spikes are binary. For a fair comparison, we compare the energy consumption of processing a single image with the same architecture of the backbones.

For ANN, we record the total number of floating-point operations (FLOPs). For SNN, we record the total number of synapse operations (SynOps), which counts the AC operations triggered by fired spikes. We follow the work Horowitz [2014] on energy consumption analysis, using a 45nm chip as a reference. According to Horowitz [2014], in a 32-bit floating-point MAC operation, the multiplication consumes 3.7pJ, the addition consumes 0.9pJ, and hence a single MAC operation consumes 4.6pJ. In contrast, a 32-bit integer AC operation consumes 0.1pJ. TABLE 9 provides the energy consumption analysis for the three backbone architectures used in this work for both ANN and SNN. It can be seen that SNN has a tremendous advantage over its ANN counterpart in energy efficiency. Across different backbone architectures, SNN can achieve about two orders of magnitude higher energy efficiency when deployed on neuromorphic hardware.

5 Conclusion

To fully leverage the advantages of brain-inspired computing for on-device remote sensing image processing, this work proposed an SNN based online adaptation framework, with application to the classification, semantic segmentation and detection tasks. We proposed an efficient unsupervised online adaptation method for SNN, in which approximate BPTT algorithm is adopted to reduce the computational complexity. Moreover, an adaptive activation scaling scheme is proposed to enhance the adaptation performance of SNN. Furthermore, a confidence-based instance weighting scheme is designed to improve the adaptation performance on the more challenging detection task. Extensive experiments on

seven remote sensing datasets, encompassing classification, semantic segmentation and detection tasks, demonstrated the effectiveness of the proposed method and its advantages over ANN methods.

Considering the energy efficiency advantage of SNN, these results show a promising prospect of the deployment of SNN-based online adaptive learning methods on edge-devices with limited computing resources. In the future, with the development of neuromorphic computing hardware and dedicated chips for SNNs, the proposed method can be deployed on such dedicated hardware to efficiently run on edge-devices, such as on on-orbit satellites and high-altitude drones. By utilizing adaptive SNN algorithms to process remote sensing images directly on edge-devices, the perception capabilities of remote sensing equipment can be greatly enhanced.

References

Ying Guo, Bin Fan, Yan Feng, Xiuping Jia, and Mingyi He. Distribution-aware and class-adaptive aggregation for few-shot hyperspectral image classification. *IEEE Transactions on Geoscience and Remote Sensing*, 2024.

Yuqun Yang, Xu Tang, Xiangrong Zhang, Jingjing Ma, Fang Liu, Xiuping Jia, and Licheng Jiao. Semi-supervised multiscale dynamic graph convolution network for hyperspectral image classification. *IEEE Transactions on Neural Networks and Learning Systems*, 2022.

Yuanhao Zhao, Genyun Sun, Ziyian Ling, Aizhu Zhang, and Xiuping Jia. Point based weakly supervised deep learning for semantic segmentation of remote sensing images. *IEEE Transactions on Geoscience and Remote Sensing*, pages 1–1, 2024. doi:10.1109/TGRS.2024.3409903.

Wei Han, Jun Li, Sheng Wang, Xinyu Zhang, Yusen Dong, Runyu Fan, Xiaohan Zhang, and Lizhe Wang. Geological remote sensing interpretation using deep learning feature and an adaptive multisource data fusion network. *IEEE Transactions on Geoscience and Remote Sensing*, 60:1–14, 2022.

Man Zhou, Jie Huang, Keyu Yan, Danfeng Hong, Xiuping Jia, Jocelyn Chanussot, and Chongyi Li. A general spatial-frequency learning framework for multimodal image fusion. *IEEE Transactions on Pattern Analysis and Machine Intelligence*, 2024.

Xiangrong Zhang, Tianyang Zhang, Guanchun Wang, Peng Zhu, Xu Tang, Xiuping Jia, and Licheng Jiao. Remote sensing object detection meets deep learning: A metareview of challenges and advances. *IEEE Geoscience and Remote Sensing Magazine*, 2023a.

Jiaqing Zhang, Jie Lei, Weiyi Xie, Yunsong Li, Geng Yang, and Xiuping Jia. Guided hybrid quantization for object detection in remote sensing imagery via one-to-one self-teaching. *IEEE Transactions on Geoscience and Remote Sensing*, 2023b.

Jiawei Zhang. Basic neural units of the brain: neurons, synapses and action potential. *arXiv preprint arXiv:1906.01703*, 2019.

Biswa Sengupta and Martin B Stemmler. Power consumption during neuronal computation. *Proceedings of the IEEE*, 102(5):738–750, 2014.

Shiva Subbulakshmi Radhakrishnan, Amritanand Sebastian, Aaryan Oberoi, Sarbassis Das, and Saptarshi Das. A biomimetic neural encoder for spiking neural network. *Nature Communications*, 12(1):2143, 2021.

Robert Kim and Terrence J Sejnowski. Strong inhibitory signaling underlies stable temporal dynamics and working memory in spiking neural networks. *Nature Neuroscience*, 24(1):129–139, 2021.

Qingyan Meng, Mingqing Xiao, Shen Yan, Yisen Wang, Zhouchen Lin, and Zhi-Quan Luo. Towards memory-and time-efficient backpropagation for training spiking neural networks. In *Proceedings of the IEEE/CVF International Conference on Computer Vision*, pages 6166–6176, 2023.

Yuhang Li, Yufei Guo, Shanghang Zhang, Shikuang Deng, Yongqing Hai, and Shi Gu. Differentiable spike: Rethinking gradient-descent for training spiking neural networks. *Advances in Neural Information Processing Systems*, 34: 23426–23439, 2021.

Bojian Yin, Federico Corradi, and Sander M Bohté. Accurate and efficient time-domain classification with adaptive spiking recurrent neural networks. *Nature Machine Intelligence*, 3(10):905–913, 2021.

Mingqing Xiao, Qingyan Meng, Zongpeng Zhang, Di He, and Zhouchen Lin. Online training through time for spiking neural networks. *Advances in Neural Information Processing Systems*, 35:20717–20730, 2022.

Wei Fang, Zhaofei Yu, Zhaokun Zhou, Ding Chen, Yanqi Chen, Zhengyu Ma, Timothée Masquelier, and Yonghong Tian. Parallel spiking neurons with high efficiency and ability to learn long-term dependencies. *Advances in Neural Information Processing Systems*, 36, 2024.

Shikuang Deng, Yuhang Li, Shanghang Zhang, and Shi Gu. Temporal efficient training of spiking neural network via gradient re-weighting. *arXiv preprint arXiv:2202.11946*, 2022.

Wei Fang, Yanqi Chen, Jianhao Ding, Zhaofei Yu, Timothée Masquelier, Ding Chen, Liwei Huang, Huihui Zhou, Guoqi Li, and Yonghong Tian. Spikingjelly: An open-source machine learning infrastructure platform for spike-based intelligence. *Science Advances*, 9(40):eadi1480, 2023.

Yujie Wu, Lei Deng, Guoqi Li, Jun Zhu, and Luping Shi. Spatio-temporal backpropagation for training high-performance spiking neural networks. *Frontiers in neuroscience*, 12:331, 2018.

Hanle Zheng, Yujie Wu, Lei Deng, Yifan Hu, and Guoqi Li. Going deeper with directly-trained larger spiking neural networks. In *Proceedings of the AAAI Conference on Artificial Intelligence*, volume 35, pages 11062–11070, 2021.

Seijoon Kim, Seongsik Park, Byunggook Na, and Sungroh Yoon. Spiking-yolo: spiking neural network for energy-efficient object detection. In *Proceedings of the AAAI Conference on Artificial Intelligence*, volume 34, pages 11270–11277, 2020.

Youngeun Kim, Joshua Chough, and Priyadarshini Panda. Beyond classification: Directly training spiking neural networks for semantic segmentation. *Neuromorphic Computing and Engineering*, 2(4):044015, 2022.

Jibin Wu, Emre Yilmaz, Malu Zhang, Haizhou Li, and Kay Chen Tan. Deep spiking neural networks for large vocabulary automatic speech recognition. *Frontiers in neuroscience*, 14:513257, 2020.

Karolina Mateńcuk, Agata Kozina, Aleksandra Markowska, Kateryna Czerniachowska, Klaudia Kaczmarczyk, Paweł Golec, Marcin Hernes, Krzysztof Lutosławski, Adrianna Kozierkiewicz, Marcin Pietranik, et al. Financial time series forecasting: Comparison of traditional and spiking neural networks. *Procedia Computer Science*, 192:5023–5029, 2021.

Yang Liu, Kejing Cao, Rui Li, Hongxia Zhang, and Liming Zhou. Hyperspectral image classification of brain-inspired spiking neural network based on approximate derivative algorithm. *IEEE Transactions on Geoscience and Remote Sensing*, 60:1–16, 2022a.

Yang Liu, Kejing Cao, Ruiyi Wang, Meng Tian, and Yi Xie. Hyperspectral image classification of brain-inspired spiking neural network based on attention mechanism. *IEEE Geoscience and Remote Sensing Letters*, 19:1–5, 2022b.

Yanhua Pang, Libo Yao, Yiping Luo, Chengguo Dong, Qinglei Kong, and Bo Chen. Repsvit: An efficient vision transformer based on spiking neural networks for object recognition in satellite on-orbit remote sensing images. *IEEE Transactions on Geoscience and Remote Sensing*, 62:1–16, 2024.

Yansheng Li, Yongjun Zhang, Xin Huang, and Jiayi Ma. Learning source-invariant deep hashing convolutional neural networks for cross-source remote sensing image retrieval. *IEEE Transactions on Geoscience and Remote Sensing*, 56(11):6521–6536, 2018.

Wei Xiong, Yafei Lv, Xiaohan Zhang, and Yaqi Cui. Learning to translate for cross-source remote sensing image retrieval. *IEEE Transactions on Geoscience and Remote Sensing*, 58(7):4860–4874, 2020.

Jingjing Ma, Duanpeng Shi, Xu Tang, Xiangrong Zhang, Xiao Han, and Licheng Jiao. Cross-source image retrieval based on ensemble learning and knowledge distillation for remote sensing images. In *IEEE International Geoscience and Remote Sensing Symposium IGARSS*, pages 2803–2806, 2021.

Jie Chen, Jingru Zhu, Ya Guo, Geng Sun, Yi Zhang, and Min Deng. Unsupervised domain adaptation for semantic segmentation of high-resolution remote sensing imagery driven by category-certainty attention. *IEEE Transactions on Geoscience and Remote Sensing*, 60:1–15, 2022.

Liang Yan, Bin Fan, Hongmin Liu, Chunlei Huo, Shiming Xiang, and Chunhong Pan. Triplet adversarial domain adaptation for pixel-level classification of vhr remote sensing images. *IEEE Transactions on Geoscience and Remote Sensing*, 58(5):3558–3573, 2019.

Meijuan Yang, Licheng Jiao, Biao Hou, Fang Liu, and Shuyuan Yang. Selective adversarial adaptation-based cross-scene change detection framework in remote sensing images. *IEEE Transactions on Geoscience and Remote Sensing*, 59(3):2188–2203, 2020.

Larry F Abbott. Theoretical neuroscience rising. *Neuron*, 60(3):489–495, 2008.

Alan L Hodgkin and Andrew F Huxley. A quantitative description of membrane current and its application to conduction and excitation in nerve. *The Journal of physiology*, 117(4):500, 1952.

Eugene M Izhikevich. Simple model of spiking neurons. *IEEE Transactions on Neural Networks*, 14(6):1569–1572, 2003.

Emre O Neftci, Hesham Mostafa, and Friedemann Zenke. Surrogate gradient learning in spiking neural networks: Bringing the power of gradient-based optimization to spiking neural networks. *IEEE Signal Processing Magazine*, 36(6):51–63, 2019.

Yangfan Hu, Qian Zheng, Xudong Jiang, and Gang Pan. Fast-snn: fast spiking neural network by converting quantized ann. *IEEE Transactions on Pattern Analysis and Machine Intelligence*, 2023.

Jibin Wu, Chenglin Xu, Xiao Han, Daquan Zhou, Malu Zhang, Haizhou Li, and Kay Chen Tan. Progressive tandem learning for pattern recognition with deep spiking neural networks. *IEEE Transactions on Pattern Analysis and Machine Intelligence*, 44(11):7824–7840, 2021.

José Antonio Pérez-Carrasco, Bo Zhao, Carmen Serrano, Begona Acha, Teresa Serrano-Gotarredona, Shouchun Chen, and Bernabé Linares-Barranco. Mapping from frame-driven to frame-free event-driven vision systems by low-rate rate coding and coincidence processing—application to feedforward convnets. *IEEE Transactions on Pattern Analysis and Machine Intelligence*, 35(11):2706–2719, 2013.

Bing Han, Gopalakrishnan Srinivasan, and Kaushik Roy. Rmp-snn: Residual membrane potential neuron for enabling deeper high-accuracy and low-latency spiking neural network. In *Proceedings of the IEEE/CVF Conference on Computer Vision and Pattern Recognition*, pages 13558–13567, 2020.

Tong Bu, Wei Fang, Jianhao Ding, PENGLIN DAI, Zhaofei Yu, and Tiejun Huang. Optimal ann-snn conversion for high-accuracy and ultra-low-latency spiking neural networks. In *International Conference on Learning Representations*, 2023.

Abien Fred Agarap. Deep learning using rectified linear units (relu). *arXiv preprint arXiv:1803.08375*, 2018.

Jian Liang, Dapeng Hu, and Jiashi Feng. Do we really need to access the source data? source hypothesis transfer for unsupervised domain adaptation. In *International Conference on Machine Learning*, pages 6028–6039, 2020.

Jian Liang, Ran He, and Tieniu Tan. A comprehensive survey on test-time adaptation under distribution shifts. *International Journal of Computer Vision*, pages 1–34, 2024.

Hao Zhao, Yuejiang Liu, Alexandre Alahi, and Tao Lin. On pitfalls of test-time adaptation. In *International Conference on Machine Learning, ICML*, 2023.

Yu Sun, Xiaolong Wang, Zhuang Liu, John Miller, Alexei Efros, and Moritz Hardt. Test-time training with self-supervision for generalization under distribution shifts. In *International Conference on Machine Learning*, pages 9229–9248, 2020a.

Yuejiang Liu, Parth Kothari, Bastien Van Delft, Baptiste Bellot-Gurlet, Taylor Mordan, and Alexandre Alahi. Ttt++: When does self-supervised test-time training fail or thrive? *Advances in Neural Information Processing Systems*, 34: 21808–21820, 2021.

Dequan Wang, Evan Shelhamer, Shaoteng Liu, Bruno A. Olshausen, and Trevor Darrell. Tent: Fully test-time adaptation by entropy minimization. In *International Conference on Learning Representations*, 2021.

Shuaicheng Niu, Jiaxiang Wu, Yifan Zhang, Yaofu Chen, Shijian Zheng, Peilin Zhao, and Mingkui Tan. Efficient test-time model adaptation without forgetting. In *International Conference on Machine Learning*, pages 16888–16905, 2022.

Junyuan Hong, Lingjuan Lyu, Jiayu Zhou, and Michael Spranger. Mecta: Memory-economic continual test-time model adaptation. In *International Conference on Learning Representations*, 2023.

Guillaume Bellec, Franz Scherr, Anand Subramoney, Elias Hajek, Darjan Salaj, Robert Legenstein, and Wolfgang Maass. A solution to the learning dilemma for recurrent networks of spiking neurons. *Nature Communications*, 11 (1):3625, 2020.

Yin Zhang, Mu Ye, Guiyi Zhu, Yong Liu, Pengyu Guo, and Junhua Yan. Ffca-yolo for small object detection in remote sensing images. *IEEE Transactions on Geoscience and Remote Sensing*, 2024.

Chaojun Shi, Xian Zheng, Zhenbing Zhao, Ke Zhang, Zibo Su, and Qiaochu Lu. Lskf-yolo: Large selective kernel feature fusion network for power tower detection in high-resolution satellite remote sensing images. *IEEE Transactions on Geoscience and Remote Sensing*, 2024.

Qin Zou, Lihao Ni, Tong Zhang, and Qian Wang. Deep learning based feature selection for remote sensing scene classification. *IEEE Geoscience and remote sensing letters*, 12(11):2321–2325, 2015.

Dengxin Dai and Wen Yang. Satellite image classification via two-layer sparse coding with biased image representation. *IEEE Geoscience and remote sensing letters*, 8(1):173–176, 2010.

Gui-Song Xia, Jingwen Hu, Fan Hu, Baoguang Shi, Xiang Bai, Yanfei Zhong, Liangpei Zhang, and Xiaoqiang Lu. Aid: A benchmark data set for performance evaluation of aerial scene classification. *IEEE Transactions on Geoscience and Remote Sensing*, 55(7):3965–3981, 2017.

Zhenfeng Shao, Ke Yang, and Weixun Zhou. Performance evaluation of single-label and multi-label remote sensing image retrieval using a dense labeling dataset. *Remote Sensing*, 10(6):964, 2018.

Zhenfeng Shao, Weixun Zhou, Xueqing Deng, Maoding Zhang, and Qimin Cheng. Multilabel remote sensing image retrieval based on fully convolutional network. *IEEE Journal of Selected Topics in Applied Earth Observations and Remote Sensing*, 13:318–328, 2020.

Bindita Chaudhuri, Begüm Demir, Subhasis Chaudhuri, and Lorenzo Bruzzone. Multilabel remote sensing image retrieval using a semisupervised graph-theoretic method. *IEEE Transactions on Geoscience and Remote Sensing*, 56(2):1144–1158, 2017.

Huiming Sun, Yuwei Lin, Qin Zou, Shaoyue Song, Jianwu Fang, and Hongkai Yu. Convolutional neural networks based remote sensing scene classification under clear and cloudy environments. In *Proceedings of the IEEE/CVF International Conference on Computer Vision*, pages 713–720, 2021.

Weipeng Shi, Wenhui Qin, Zhonghua Yun, Allshine Chen, Kai Huang, and Tao Zhao. Land cover classification in foggy conditions: Toward robust models. *IEEE Geoscience and Remote Sensing Letters*, 19:1–5, 2022.

Runou Yang. Adverse weather simulation. <https://github.com/RicardooYoung/AdverseWeatherSimulation>, 2023.

Karen Simonyan and Andrew Zisserman. Very deep convolutional networks for large-scale image recognition. *arXiv preprint arXiv:1409.1556*, 2014.

Kaiming He, Xiangyu Zhang, Shaoqing Ren, and Jian Sun. Deep residual learning for image recognition. In *Proceedings of the IEEE Conference on Computer Vision and Pattern Recognition*, pages 770–778, 2016.

Jonathan Long, Evan Shelhamer, and Trevor Darrell. Fully convolutional networks for semantic segmentation. In *Proceedings of the IEEE Conference on Computer Vision and Pattern Recognition*, pages 3431–3440, 2015.

Joseph Redmon and Ali Farhadi. Yolov3: An incremental improvement. *arXiv preprint arXiv:1804.02767*, 2018.

Yu Sun, Xiaolong Wang, Zhuang Liu, John Miller, Alexei Efros, and Moritz Hardt. Test-time training with self-supervision for generalization under distribution shifts. In *International Conference on Machine Learning*, pages 9229–9248. PMLR, 2020b.

Yaroslav Ganin and Victor Lempitsky. Unsupervised domain adaptation by backpropagation. In *International Conference on Machine Learning*, pages 1180–1189. PMLR, 2015.

Steffen Schneider, Evgenia Rusak, Luisa Eck, Oliver Bringmann, Wieland Brendel, and Matthias Bethge. Improving robustness against common corruptions by covariate shift adaptation. *Advances in Neural Information Processing Systems*, 33:11539–11551, 2020.

Dequan Wang, Evan Shelhamer, Shaoteng Liu, Bruno Olshausen, and Trevor Darrell. Tent: Fully test-time adaptation by entropy minimization. *arXiv preprint arXiv:2006.10726*, 2020.

Yi-Hsuan Tsai, Wei-Chih Hung, Samuel Schulter, Kihyuk Sohn, Ming-Hsuan Yang, and Manmohan Chandraker. Learning to adapt structured output space for semantic segmentation. In *Proceedings of the IEEE Conference on Computer Vision and Pattern Recognition*, pages 7472–7481, 2018.

Tuan-Hung Vu, Himalaya Jain, Maxime Bucher, Matthieu Cord, and Patrick Pérez. Advent: Adversarial entropy minimization for domain adaptation in semantic segmentation. In *Proceedings of the IEEE/CVF Conference on Computer Vision and Pattern Recognition*, pages 2517–2526, 2019.

Vibashan VS, Poojan Oza, and Vishal M Patel. Towards online domain adaptive object detection. In *Proceedings of the IEEE/CVF Winter Conference on Applications of Computer Vision*, pages 478–488, 2023.

Mark Horowitz. 1.1 computing’s energy problem (and what we can do about it). In *IEEE International Solid-State Circuits Conference Digest of Technical Papers (ISSCC)*, pages 10–14, 2014.